JGR Solid Earth

RESEARCH ARTICLE
10.1029/2018JB017103

Noneruptive Unrest at the Caldera of Alcedo Volcano (Galápagos Islands) Revealed by InSAR Data and Geodetic Modeling

Federico Galetto[1], Marco Bagnardi[2,3], Valerio Acocella[1], and Andrew Hooper[2]

[1]Dipartimento di Scienze, Università degli Studi di Roma Tre, Rome, Italy, [2]COMET, School of Earth and Environment, University of Leeds, Leeds, UK, [3]Now at Jet Propulsion Laboratory, California Institute of Technology, Pasadena, CA, USA

Key Points:
- The 2007-2011 noneruptive unrest at Alcedo was caused by shallow emplacement of new magma with limited lateral intrusion
- Uplift during unrest is similar in location and shape to the longer-term weak resurgence of the caldera
- This unrest provides the rare opportunity to document the incremental growth of a basaltic resurgent caldera

Supporting Information:
- Supporting Information S1

Correspondence to:
F. Galetto,
federico.galetto@uniroma3.it

Citation:
Galetto, F., Bagnardi, M., Acocella, V., & Hooper, A. (2019). Noneruptive unrest at the caldera of Alcedo Volcano (Galápagos Islands) revealed by InSAR data and geodetic modeling. *Journal of Geophysical Research: Solid Earth*, *124*, 3365–3381. https://doi.org/10.1029/2018JB017103

Received 28 NOV 2018
Accepted 8 FEB 2019
Accepted article online 13 FEB 2019
Published online 4 APR 2019

Abstract Understanding volcanic unrest is crucial to forecasting eruptions. At active mafic calderas unrest culminates in eruption more frequently than at felsic calderas. However, the mafic caldera of Alcedo Volcano (Ecuador) has experienced repeated episodes of unrest without erupting, since at least 1992, when geodetic monitoring began. Here we investigate the unrest that occurred between 2007 and 2011 using interferometric synthetic aperture radar (InSAR) data and geodetic modeling. We observe an initial asymmetric uplift of the southern caldera floor (~30 cm of vertical motion) from 2007 to 2009, followed by subsidence of the uplifted area and contemporary uplift of the northwestern caldera rim between January and June 2010. Finally, from June 2010 through March 2011, caldera uplift resumed. The first uplift episode is best explained by inflation of a sill and the activation of an inner ring fault. Successive caldera subsidence and rim uplift are compatible with the withdrawal of magma from the previously inflated sill and its northwestern migration. The resumption of uplift is consistent with the repressurization of the sill. This evolution suggests episodic magma emplacement in a shallow reservoir beneath the caldera, with aborted lateral magma migration, probably due to the discontinuous supply from depth. This short-term deformation pattern matches well geological observations showing a longer-term (hundreds of years at least) asymmetric uplift of the caldera floor, culminating in a weak resurgence of ~30 m. We propose that the monitored episodes of uplift represent short-term stages of the rarely observed incremental growth of a resurgent basaltic caldera.

1. Introduction

Calderas are broad subcircular depressions resulting from the partial or complete emptying of a subsurface magma reservoir as a consequence of an eruption or lateral migration of magma, as observed in 1968 at Fernandina (Galápagos, Ecuador) and in 2014–2015 at Bardarbunga Volcano, Iceland (Gudmundsson et al., 2016; Howard et al., 2018). Most active calderas experience periods of unrest over decadal timescales (Newhall & Dzurisin, 1988; Acocella et al., 2015), where unrest is defined as a deviation from baseline monitoring parameters, such as changes in seismicity, degassing, and ground deformation. While not all episodes of unrest culminate in an eruption, most eruptions, especially in caldera systems, are preceded by a period of unrest. Therefore, understanding the nature of an episode of volcanic unrest is fundamental when assessing volcanic hazard (Biggs et al., 2014; Acocella et al., 2015; Biggs & Pritchard, 2017). This effort should be pursued regardless of whether the unrest results in eruption or not. In fact, it is equally important to understand both processes leading to eruptions and those that do not; the impact in forecasting eruptions is equally significant in both cases.

Previous studies have shown that unrest at mafic calderas is generally more regular, or "predictable," than at felsic calderas (Dvorak & Dzurisin, 1997; Acocella et al., 2015). At mafic calderas, preeruptive inflation and increase in seismicity are commonly followed by an eruption and coeruptive deflation (Dvorak & Dzurisin, 1997; Acocella et al., 2015), over multiple self-similar cycles. On the other hand, felsic calderas often show subsequent periods of inflation and increase in seismicity that do not culminate into eruptions (Acocella et al., 2015; Sandri et al., 2017). This basic distinction, however, includes many exceptions, such as mafic calderas that experience multiple episodes of noneruptive unrest, a behavior more characteristic of felsic systems. Among these is the mafic caldera of Alcedo Volcano (Isabela Island, Galápagos,

Ecuador), where previous geophysical measurements have identified periods of unrest without eruptions. Our understanding of these noneruptive unrest episodes remains limited (Amelung et al., 2000; Hooper et al., 2007), despite being of fundamental importance for the definition of the mechanisms hindering the rise of magma to the surface and for our capability of forecasting eruptions.

In this study we use interferometric synthetic aperture radar (InSAR) data acquired at Alcedo between 2006 and 2011, which record surface displacements during multiple deformation events that did not end with an eruption and that have similar characteristics to episodes of noneruptive unrest that occurred between 1992 and 2001 (Amelung et al., 2000; Hooper et al., 2007). Through modeling the geodetic data, we place constraints on the sources responsible for these episodes of unrest. In addition, we link these shorter-term episodes to the longer-term evolution of the caldera, where geological and geomorphological observations suggest the development of a weak resurgence.

2. Geological Background: Galápagos and Alcedo

Alcedo Volcano lies in the Galápagos Archipelago, a widespread (> 40,000 km^2) system of volcanic islands and seamounts in the eastern Pacific Ocean, and one of the most active magmatic provinces. Galápagos volcanism is related to a hot spot, whose head is centered below the western islands of the archipelago, immediately to the SW of Fernandina Island (Naumann & Geist, 2000; Hooft et al., 2003; Gibson & Geist, 2010; Villagómez et al., 2014). The Galápagos islands and seamounts have grown above a broad and thick platform, which overlays young (<10 Ma) oceanic lithosphere (Feighner & Richards, 1994; Rychert et al., 2014). The Galápagos Archipelago is located on the eastward moving Nazca plate, ~170 km south of the Galápagos Spreading Center (GSC), an E-W striking intermediate-rate spreading center, which separates the Cocos (to the north) and Nazca (to the south) plates (Figure 1a; Canales et al., 1997, 2002; Werner et al., 2003; Mittelstaedt et al., 2012; Harpp & Geist, 2018). The NW-SE trending Darwin-Wolf lineament separates the eastern from the western Galápagos, which are two distinct volcanological, petrological, geochemical, and structural provinces (Figure 1a; Feighner & Richards, 1994; Harpp & Geist, 2018; White et al., 1993). The younger western Galápagos are characterized by large and flexurally supported shield volcanoes with summit calderas, while the older eastern Galápagos volcanoes are smaller and do not have well-developed calderas (Feighner & Richards, 1994; Harpp & Geist, 2018).

Most of the recent volcanic activity in the Galápagos has focused on the seven shield volcanoes forming the western islands of Isabela and Fernandina, near the upwelling region of the hot spot (Gibson & Geist, 2010; Villagómez et al., 2014). These volcanoes are Fernandina, Ecuador, Wolf, Darwin, Alcedo, Sierra Negra, and Cerro Azul (the coalescence of the last six volcanoes makes up Isabela Island; Figure 1b). Western Galápagos volcanoes have gently sloping outer flanks, steep upper flanks, and well-established summit calderas (Mouginis-Mark et al., 1996; Munro & Rowland, 1996; Naumann & Geist, 2000). With the exception of Cerro Azul, all these volcanoes have shown evidence for shallow (1–3 km beneath the caldera floor) flat-topped magma reservoirs (Geist et al., 2014, and references therein).

The western Galápagos volcanoes have been classified into three evolutionary stages (Geist et al., 2014; Harpp & Geist, 2018): (1) juvenile transient phase (e.g., Cerro Azul), with a deep, hot, and small magmatic system; (2) mature steady state phase (e.g., Fernandina, Darwin, and Wolf), characterized by high magma supply rates and a well-developed, thermochemically buffered, thick mush zones with a shallow, flat top; and (3) dying cooling phase (e.g., Alcedo), with a cooler, less fed, and more evolved magmatic system. The dying phase of Alcedo is supported by a decrease in eruption rate since ~120 ka, from 1.8×10^6 to 0.1×10^6 m^3/year (Geist et al., 1994). In addition, even if Alcedo mainly erupts transitional basalts, at ~120 ka it erupted rhyolitic pumice and lava, which are the most fractionated and evolved products in the western Galápagos (Geist et al., 1995).

The volcanic edifice of Alcedo reaches a maximum elevation of 1,130 m above sea level, with gently dipping lower flanks, steeper upper flanks (33°), and a large (41.6 km^2) but shallow caldera (270 m deep). This morphology has been related to a decrease in magmatic activity (Geist et al., 1994; Mouginis-Mark et al., 1996; Munro & Rowland, 1996; Naumann & Geist, 2000; Nordlie, 1973). The caldera is elliptical in shape (7 × 6 km) and has its major axis oriented NW-SE (Munro & Rowland, 1996) (Figure 1c). Alcedo caldera shows a complex morphology, with three fault scarps delimiting the NW side and one scarp in the SSW

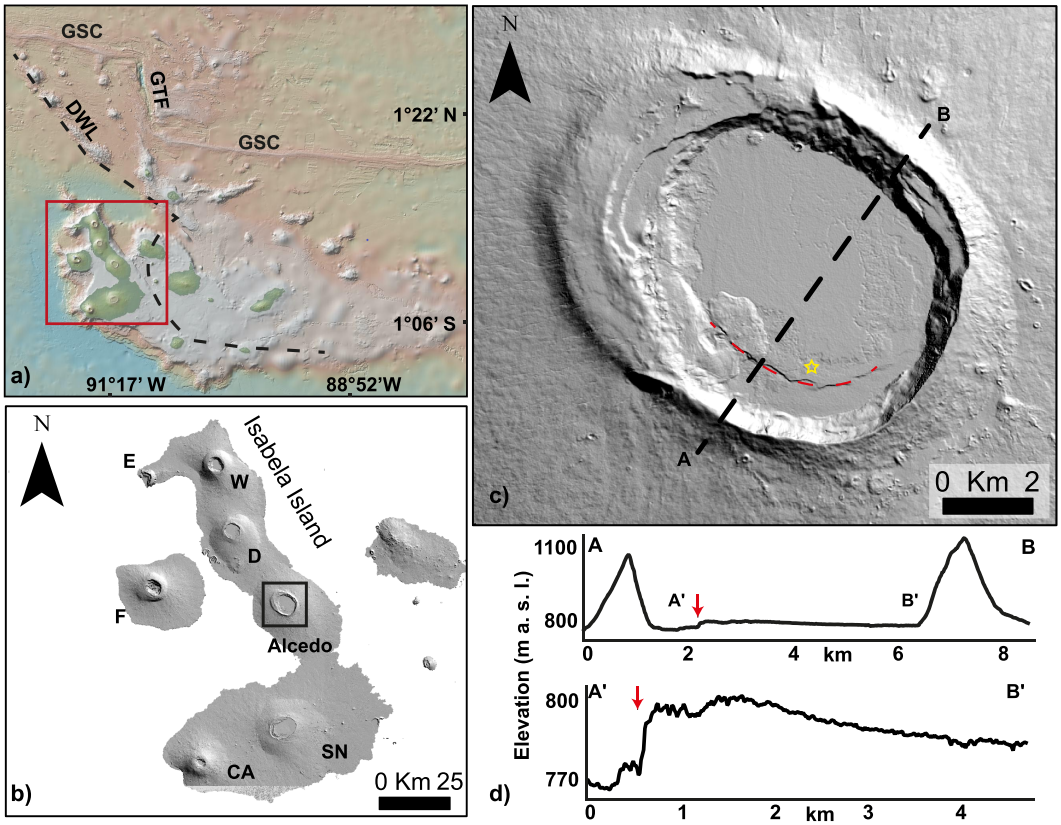

Figure 1. (a) Topography and bathymetry of the Galápagos Archipelago. GSC = Galápagos Spreading Center; GTF = Galápagos Transform Fault; the dashed line marks the Darwin-Wolf lineament (DWL) separating western and eastern Galápagos, as traced by Feighner and Richards (1994) (digital elevation model from GeoMappApp). The red square outlines the extent of panel (b). (b) Shaded relief map (from WorldDEM data) of Fernandina (F) and Isabela Islands, on which lie the volcanoes Ecuador (E), Wolf (W), Darwin (D), Alcedo (the black square outlines the extent of panel (c)), Sierra Negra (SN), and Cerro Azul (CA). (c) Shaded relief map of Alcedo caldera. The yellow star indicates the location for which deformation time series are shown in Figures 2c, 2d, 2j, and 2k. The red dashed line marks the southern intracaldera fault. The black dashed line A-B marks the location of the topographic profile in panel (d). (d) Topographic profile across the caldera floor (A-B profile) and the snapshot (A′-B′ profile) that highlights the uplift, or weak resurgence, of the southern part. Elevation is with respect to sea level. The red arrows point the location of the southern intracaldera fault.

part. The scarps to the NW have been interpreted as blocks of the caldera floor that have been broken and faulted during repeated cycles of caldera collapse and filling, with the center of the collapse progressively migrating southward. This migration may reflect that of a shallow magma reservoir, which therefore would currently lie below the southern part of the caldera floor (Geist et al., 1994). The SSW intracaldera ring fault system is responsible for the formation of the caldera moat and of the trapdoor uplift of the southern caldera floor (Figures 1c and 1d). Such an uplift, reaching ~30 m, indicates a weak resurgence of the caldera (Geist et al., 1994), a feature rarely observed at mafic calderas, but that it is also occurring at the nearby mafic caldera of Sierra Negra (Galetto et al., 2017). This ring fault has been interpreted as an older caldera fault reactivated with opposite motion during the uplift, or resurgence (Geist et al., 1994). This area is also characterized by intense fumarolic activity, fed by a shallow geothermal system located below the SW sector of the caldera (Goff et al., 2000). In this sector two phreatic explosions occurred between 1993 and 1994 (Green, 1994).

The last recorded magmatic eruption occurred in the mid-1900s (Geist et al., 1994, 1995). In recent decades, geophysical measurements have shown that Alcedo experienced repeated episodes of noneruptive unrest. Between 1992 and 1997, InSAR data showed a > 90-cm net uplift, mainly focused on the southern part of the caldera (Amelung et al., 2000; Hooper et al., 2007). Such data, however, offer poor temporal sampling and are not sufficient to determine if the uplift occurred episodically or at a stable rate throughout the 6-year interval. Successively, between 1997 and 2001, uplift switched to subsidence (<11 cm), which has been interpreted as deflation of an ellipsoid-like body at ~2.2 km below sea level (Hooper et al., 2007). Conversely to

Cerro Azul, Fernandina, and Wolf (Amelung et al., 2000; Bagnardi et al., 2013; Stock et al., 2018; Xu et al., 2016), no deformation is recorded outside the caldera of Alcedo in the last 30 years.

3. Data and Methods

To measure surface deformation at Alcedo, we processed 83 synthetic aperture radar images acquired by the European Space Agency's ENVISAT satellite (C-band, wavelength $\lambda = 5.63$ cm), 35 from an ascending track (T61) acquired between January 2006 and May 2010 and 48 from a descending track (T140) acquired between January 2003 and May 2010 (Figure 2). We also processed 38 synthetic aperture radar images from the Japanese Space Agency's ALOS-1 satellite (L-band, wavelength $\lambda = 23.6$ cm), 20 from an ascending track (T133) acquired between January 2007 and March 2011 and 18 from a descending track (T474) acquired between January 2007 and July 2010 (Figure 2).

Interferograms were formed using the InSAR Scientific Computing Environment (ISCE) software (Rosen et al., 2012) and by applying conventional differential InSAR processing techniques. Topographic contributions to the interferometric phase were removed using a 30-m-resolution digital elevation model from the NASA Shuttle Radar Topography Mission (Farr et al., 2007). Interferograms were then combined to study the temporal evolution of surface displacements through a multitemporal approach. We applied the Small Baseline method using the StaMPS software (Hooper, 2008; Hooper et al., 2012) and selected the processing parameters that maximized the signal-to-noise ratio. In supporting information Figure S1 we show the optimal networks of interferograms used for the Small Baseline analyses plotted as a function of their perpendicular and temporal baselines. Finally, we used the method of Wright et al. (2004) to convert the ALOS-1 satellite line-of-sight (LOS) displacements from two different viewing geometries into vertical and horizontal (E-W) components of displacement (Figure 3).

To constrain the sources of deformation, we inverted the ALOS-1 LOS displacement measurements. These data sets, compared to the ENVISAT data, offer much denser spatial data coverage, since L-band data can maintain better coherence in vegetated areas, such as the flanks of Alcedo. We estimated deformation source parameters and uncertainties using the Bayesian approach implemented in the Geodetic Bayesian Inversion Software (GBIS; Bagnardi & Hooper, 2018). The inversion algorithm uses a Markov chain Monte Carlo method, incorporating the Metropolis-Hastings algorithm, to find the posterior probability density functions (PDFs) of model parameters. When available, the ascending and descending ALOS-1 LOS data were jointly inverted to better constrain the deformation source parameters.

Through the Bayesian approach we sampled the joint posterior PDF for the model parameters, taking into account uncertainties in the data, which were directly quantified using experimental semivariograms calculated from the data, and approximated by unbounded exponential one-dimensional functions with a nugget (Bagnardi & Hooper, 2018). Since no prior information on the source parameters was available, we set non-informative uniform prior PDFs bounded by geologically realistic values (Tables 1–3). To reduce the computational burden, InSAR data were subsampled using an adaptive quadtree method (Bagnardi & Hooper, 2018; Decriem et al., 2010). In each inversion, we sampled the posterior PDFs through 1,000,000 iterations. Depth estimates are referred to as distance from the surface.

Together with deformation source-types already implemented in GBIS (e.g., point source (Mogi, 1958), finite spherical cavity (McTigue, 1987), prolate ellipsoid (Yang et al., 1988), and rectangular dislocation (RD) with uniform opening (Okada, 1985), we tested the RD and the compound dislocation models (CDM) of Nikkhoo et al. (2017). The RD is similar to the RD with uniform opening of Okada (1985) but has full rotational degrees of freedom. The CDM is able to simulate a sill/dike of finite thickness with full rotational degrees of freedom and is free of artifact singularities (Nikkhoo et al., 2017). For all the models we assumed an isotropic elastic half-space with a Poisson's ratio $\nu = 0.25$. Under these assumptions, the estimated volume changes (ΔV) may underestimate the volume of magma that flowed in. In fact, these models do not consider the eventuality that the injection of new magma in a reservoir can be partly accommodated without surface deformation by the compression of the magmatic system (especially the gas and liquid phases) (Huppert & Woods, 2002; Voight et al., 2010), or by the viscous response of the host rock (Jellinek & DePaolo, 2003). Therefore, even though the effect of any viscous process may become significant on timescales that are longer than our data coverage (Degruyter & Huber, 2014; Jellinek & DePaolo, 2003), the volume changes presented in this study should be considered as minimum estimates.

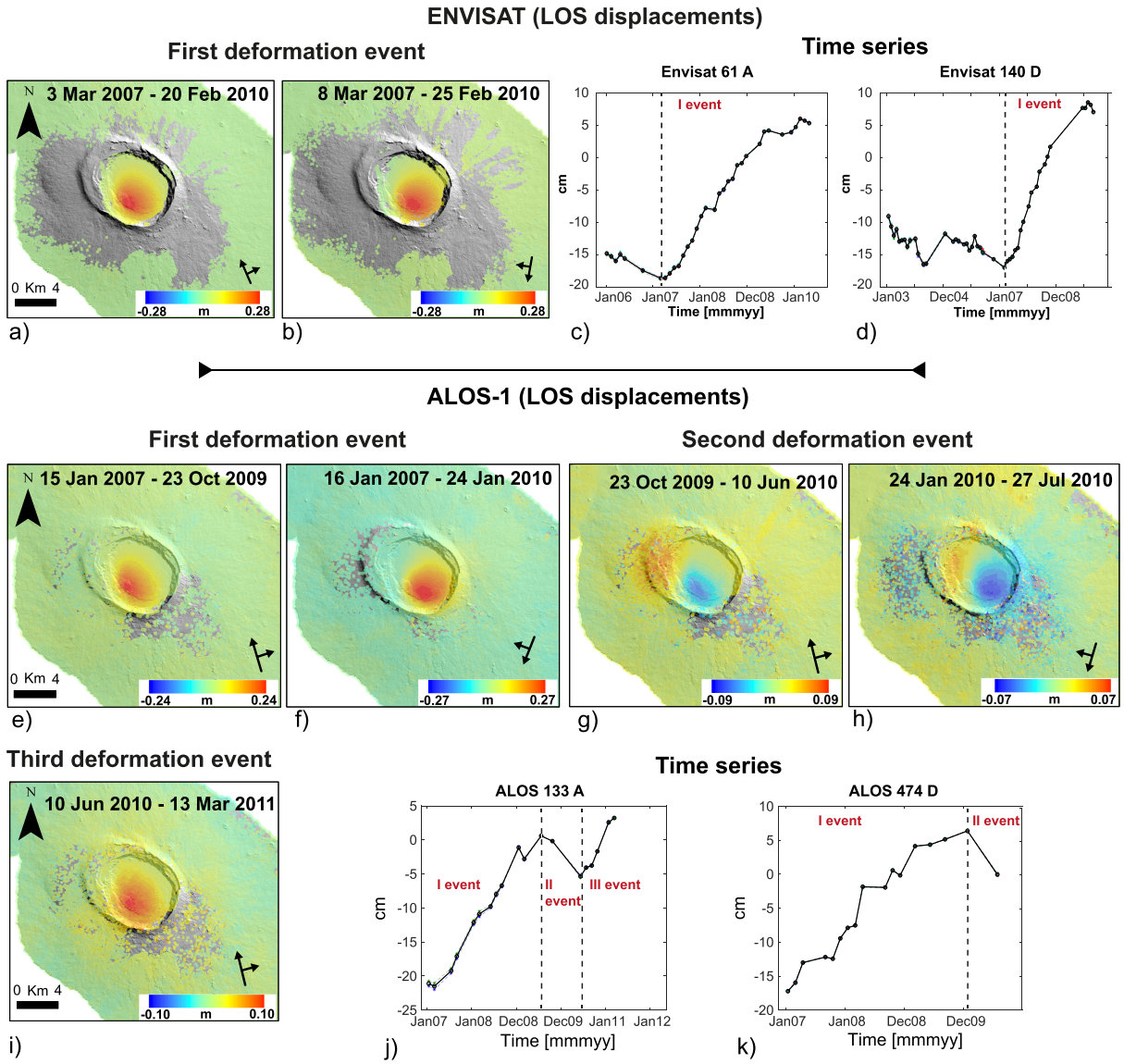

Figure 2. Time series results. ENVISAT LOS displacement map (a) for ascending orbit 61 (March 2007 to February 2010) and (b) for descending orbit 140 (March 2007 to February 2010). (c and d) ENVISAT time series (ts) (see star in Figure 1c for location). ALOS-1 LOS displacement map (e) for ascending orbit 133 (January 2007 to October 2009) and (f) for descending orbit 474 (January 2007 to January 2010). ALOS-1 LOS displacement map (g) for ascending orbit 133 (October 2009 to June 201) and (h) for descending orbit 474 (January 2010 to July 2010). (i) ALOS-1 LOS displacement map for ascending orbit 133 (June 2010 to March 2011). (j and k) ALOS-1 time series (see star in Figure 1c for location). In (a), (b), and (e)–(i) data are unwrapped, and spatially correlated look-angle errors (including orbital ramps) are removed. Displacement maps are overlaid onto shaded relief map from WorldDEM data. LOS = line-of-sight.

4. Results

4.1. Surface Deformation

From the analysis of InSAR time series calculated from ENVISAT and ALOS-1 data, we observe that the caldera of Alcedo subsided ~6 cm between the start of data coverage in 2003 and the end of 2006, with a minor, short-lived episode of uplift during the second half of 2004 (Figures 2c and 2d). From January 2007, we identify three main deformation events on which we focus our subsequent analyses.

4.1.1. First Event

From January 2007 to the end of 2009, both the ALOS-1 and ENVISAT data show a temporally linear (Figures 2c and 2d) but spatially asymmetric (Figures 2a, 2b, 2e, and 2f, Figures 3a and 3b) uplift of the southern part of the caldera. The maximum vertical displacement, ~30 cm, with a mean uplift rate of

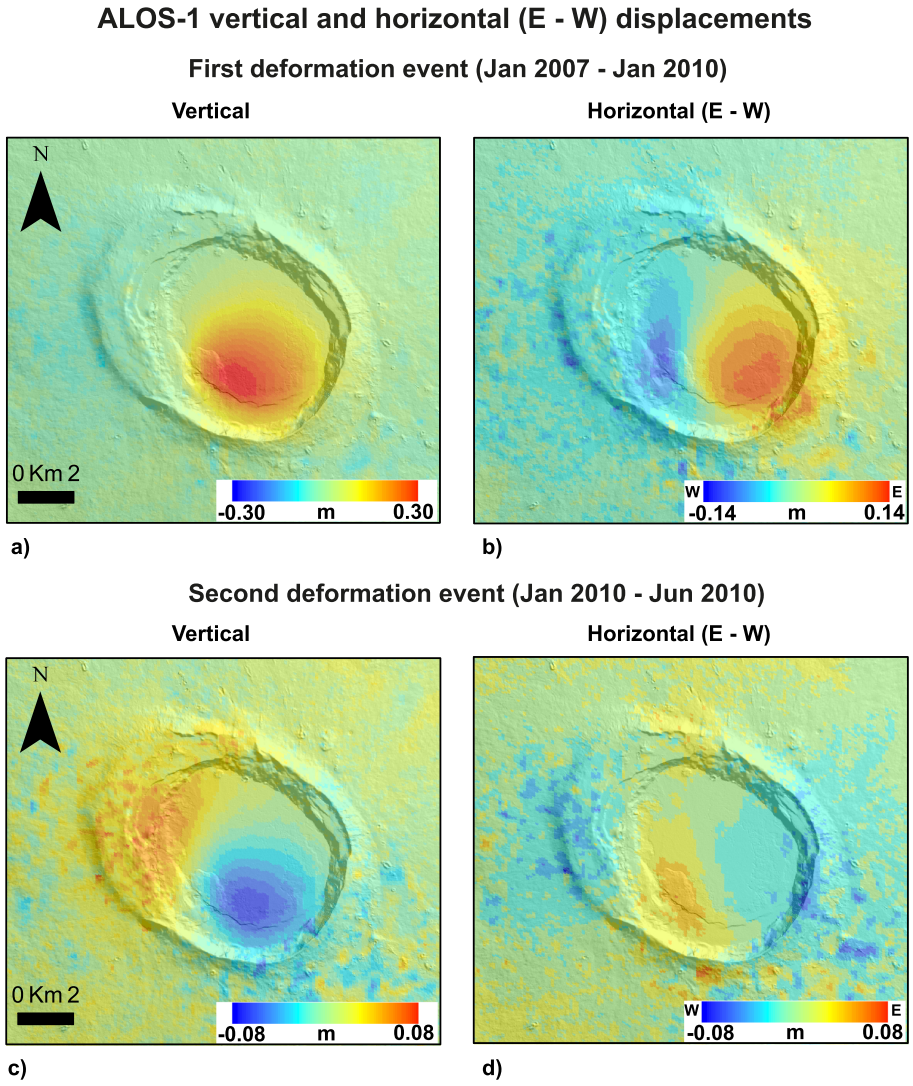

Figure 3. ALOS-1 vertical and horizontal (E-W) displacement maps from the combination of ascending and descending line-of-sight data (e.g., Wright et al., 2004). (a) Vertical and (b) horizontal displacements during the first deformation event, from January 2007 to January 2010. (c) Vertical and (d) horizontal (E-W) displacements during the second deformation event, from January 2010 to June 2010). In (b) and (d), blue colors represent westward horizontal motion and red colors eastward motion. Displacement maps are overlaid on a shaded relief map from WorldDEM data.

~8.9 cm/year, is recorded at the SW edge of the uplifted area (Figure 3a), where it is also bounded by the southern intracaldera fault (Figure 1c).

4.1.2. Second Event

From January to June 2010, ALOS-1 data show that the previously uplifted area subsided by a maximum of ~8 cm in a spatial asymmetric pattern peaking near the southern intracaldera fault (Figures 2g, 2h, 3c, and 3d), as during the first event. During the same time interval, the western portion of the caldera rim, across the three faults scarps, uplifted by up to ~5 cm.

4.1.3. Third Event

From July 2010 to March 2011, data coverage is limited to the ascending ALOS-1 track. These data show uplift of the previously subsiding area in the southern part of the caldera, corresponding to the uplifted area during the first event (Figures 2i and 2j). The maximum LOS displacement is ~10 cm, corresponding to a displacement rate of ~13 cm/year, which is ~4 cm/year higher than during the first event.

Table 1
Results of the Bayesian Analysis

	First event (CDM)										
Model	*X* (m)	*Y* (m)	*Z* (m)	*ωX*	*ωY*	*ωZ*	ax (m)	ay (m)	az (m)	Op. (m)	ΔV ($\times 10^6$ m^3)
Optimal	−7,971	5,841	2,180	−36	16	211	1,736	1,365	242	0.76	9.5
2.50%	−8,054	5,727	2,104	−40	14	209	1,655	1,230	203	0.69	8.6
97.50%	−7,888	5,928	2,316	−34	19	215	1,851	1,478	287	0.88	10.8
Lower	−10,000	3,000	2,000	−50	−30	180	800	800	4	0	
Upper	−5,000	8,000	4,000	50	40	360	4,000	4,000	500	10	
	First event (CDM + fault)										
	Fault										
	X (m)	*Y* (m)	*Z* (m)	*L* (m)	*W* (m)	Dip[a]	Strike	Rake[a]	Slip (m)		
Optimal	−8,863	5,223	1,030	1,765	908	80	122	−90	0.39		
2.50%	−8,932	5,185	854	1,562	420	80	119	−90	0.31		
97.50%	−8,802	5,308	1,071	1,942	940	80	126	−90	0.76		
Lower	−10,000	4,000	700	800	400	80	90	−90	0.1		
Upper	−5,000	6,000	1,600	2,900	950	80	180	−90	2		
	CDM										
	X (m)	*Y* (m)	*Z* (m)	*ωX*	*ωY*	*ωZ*	ax (m)	ay (m)	az (m)	Op. (m)	ΔV ($\times 10^6$ m^3)
Optimal	−7,783	5,938	2,144	−19	−15	273	1,581	1,935	214	0.57	8.7
2.50%	−7,883	5,850	2,025	−23	−19	269	1,437	1,848	104	0.52	7.5
97.50%	−7,735	5,991	2,323	−17	−12	277	1,641	2,016	252	0.68	9.6
Lower	−10,000	3,000	2,000	−50	−40	180	800	800	4	0	
Upper	−5,000	8,000	4,000	50	30	360	4,000	4,000	500	10	
	Second event (two CDM)										
	First CDM										
	X (m)	*Y* (m)	*Z* (m)	*ωX*	*ωY*	*ωZ*	ax (m)	ay (m)	az (m)	Op. (m)	ΔV ($\times 10^6$ m^3)
Optimal	−8,240	5,832	2,326	7	32	112	836	1,948	371	−0.37	−3.9
2.50%	−8,494	5,555	2,105	−11	17	109	806	1,373	138	−0.51	−5.3
97.50%	−7,755	6,328	2,815	12	47	144	1,255	2,353	578	−0.22	−2.3
Lower	−9,500	4,000	2,000	−20	0	60	800	800	1	−5	
Upper	−6,500	7,500	4,000	20	50	360	2,500	2,800	600	0	
	Second CDM										
	X (m)	*Y* (m)	*Z* (m)	*ωX*	*ωY*	*ωZ*	ax (m)	ay (m)	az (m)	Op. (m)	ΔV ($\times 10^6$ m^3)
Optimal	−10,275	7,468	2,174	15	−10	257	2,470	876	527	0.18	2.8
2.50%	−10,582	7,215	2,154	−3	−27	235	1,140	714	15	0.13	1.7
97.50%	−9,810	7,981	3,726	42	−1	292	2,743	1,523	636	0.57	4.6
Lower	−14,000	5,800	2,000	−10	−60	220	700	700	1	0	
Upper	−8,000	10,000	4,000	50	0	359	3,000	3,000	700	5	

Note. Optimal = maximum a posteriori probability solution. The percentages 2.50% and 97.50% are the lower and upper boundaries of the 95% credible intervals. Lower and Upper are the bounds of the prior distribution used for the inversion. *X* and *Y* are the local coordinates of the center of CDM and the center of the RD fault. Local coordinates origin (see Figures 4a and 4b): longitude 91°05′W and latitude 0°49′S. *Z* is the depth (with respect to the caldera floor) (positive downward). *ωZ* is the strike angle, and *ωX* and *ωY* are, respectively, the rotational angle along the *X* and *Y* directions. ax, ay, and az are the lengths of the semiaxes of the CDM along the *x*, *y*, and *z* axes, respectively (see Nikkhoo et al., 2017 for a better explanation). Op. is the opening. *L* is the length of the fault, while *W* is its width. Rake is the rake of the fault, while strike is its strike angle. Dip is the dip angle of the fault. Volume change (ΔV) has been calculated with the formula $\Delta V = 4 * (\text{opening}) * [(\text{ax} * \text{ay}) + (\text{ay} * \text{az}) + (\text{ax} * \text{az})]$ (Nikkhoo et al., 2017).
[a]Parameter held fixed.

4.2. Geodetic Modeling

For the first deformation event we tested different source geometries. Point source (Mogi, 1958), finite spheroid (McTigue, 1987), and ellipsoid (Yang et al., 1988) sources were not able to reproduce the observed displacements (Figure S2 and Table S1). A better fit to the data was instead obtained using sill-like geometries,

Table 2
Results of the Bayesian Analysis

	First event (RD)									
Model	X (m)	Y (m)	Z (m)	L (m)	W (m)	θ	Dip	Strike	Op. (m)	ΔV ($\times 10^6$ m^3)
Optimal	−8,056	5,714	2,174	3,662	2,286	−37	35	329	0.83	7
2.50%	−8,126	5,633	2,109	3,523	2,084	−41	34	326	0.77	6.5
97.50%	−7,998	5,770	2,294	3,819	2,458	−32	37	332	0.96	7.7
Lower	−11,000	2,000	2,000	800	800	−60	0	0	0	
Upper	−5,000	8,000	4,000	4,500	4,000	0	50	360	10	
	First event (RD Fault + RD)									
	Fault									
	X (m)	Y (m)	Z (m)	L (m)	W (m)	Dip[a]	Strike	Rake[a]	Slip (m)	
Optimal	−8,858	5,225	871	1,664	474	80	121	−90	0.58	
2.50%	−8,906	5,164	820	1,507	406	80	119	−90	0.35	
97.50%	−8,787	5,260	971	1,844	764	80	125	−90	0.74	
Lower	−10,000	4,000	700	800	400	80	90	−90	0.1	
Upper	−5,000	6,000	1,600	2,900	950	80	180	−90	2	
	RD									
	X (m)	Y (m)	Z (m)	L (m)	W (m)	θ	Dip	Strike	Op. (m)	ΔV ($\times 10^6$ m^3)
Optimal	−7,829	5,895	2,164	3,142	4,003	31	26	333	0.58	7.3
2.50%	−7,913	5,828	2,058	2,968	3,811	27	24	328	0.53	6.7
97.50%	−7,777	5,942	2,341	3,299	4,113	37	29	337	0.67	8.1
Lower	−11,000	2,000	2,000	800	800	0	0	240	0	
Upper	−5,000	8,000	4,000	4,400	4,500	50	50	360	10	
	Second event (two RD)									
	RD									
	X (m)	Y (m)	Z (m)	L (m)	W (m)	θ	Dip	Strike	Op. (m)	ΔV ($\times 10^6$ m^3)
Optimal	−8,282	5,866	2,675	4,380	918	14	19	294	−0.56	−2.3
2.50%	−8,582	5,582	2,322	3,245	911	−28	5	281	−0.71	−3
97.50%	−7,833	6,269	2,943	4,968	1,913	25	30	335	−0.25	−1.6
Lower	−10,000	4,000	2,100	1,000	900	−35	−1	180	−2	
Upper	−5,000	8,000	4,000	5,200	4,000	35	35	360	0	
	RD									
	X (m)	Y (m)	Z (m)	L (m)	W (m)	θ	Dip	Strike	Op. (m)	ΔV ($\times 10^6$ m^3)
Optimal	−10,029	7,562	3,080	1,331	4,083	49	23	217	0.43	2.3
2.50%	−10,537	7,251	2,788	915	2,495	5	6	195	0.21	1.5
97.50%	−9,797	8,054	3,825	2,274	5,479	59	33	256	0.96	3.2
Lower	−11,000	5,000	2,100	900	2,000	−1	−10	100	0	
Upper	−7,000	9,000	4,000	2,500	6,000	60	40	360	2	

Note. Optimal = maximum a posteriori probability solution. The percentages 2.50% and 97.50% are the lower and upper boundaries of the 95% credible intervals. Lower and Upper are the bounds of the prior distribution used for the inversion. X and Y are the local coordinates of the center of RD. Local origin coordinates (see Figures 4a and 4b): longitude 91°05′W and latitude 0°49′S. Z is the depth (with respect to the caldera floor; positive downward). θ is the angle between the RD upper edge and the intersection of the RD plane with the free surface. L and W are, respectively, the length and the width. Rake is the rake of the fault. Op. is the opening. Dip is the dip angle. Strike is the strike angle (see Nikkhoo et al., 2017 for a better explanation of all these parameters). ΔV is the volume change calculated with the formula $\Delta V = L * W *$ Op. RD = rectangular dislocation.
[a]Parameter held fixed

modeled as both CDM and RD (Figure 4). For the CDM, the model converged toward a rectangular, slightly inclined (<20°) sill, whose centroid lies at 2.2 ± 0.1 km below the southern caldera floor, with opening of 0.78 ± 0.1 m (Figures 4c–4f and Table 1). The corresponding volume change (ΔV) is 9.7 ± 1.1 × 10^{-3} km^3, with an average injection rate of 3.4 ± 0.6 × 10^{-3} km^3/year. To account for the asymmetric uplift,

Table 3
Results of the Bayesian Analysis of the Third Deformation Event Using an RD Source

Model	X (m)	Y (m)	Z (m)	L (m)	W (m)	θ	Dip	Strike	Op. (m)	ΔV ($\times 10^6$ m^3)
Optimal	−7,971	6,086	3,207	2,521	3,788	19	23	10	0.42	4.1
2.50%	−8,560	5,788	2,674	1,035	2,111	1	4	1	0.26	2.4
97.50%	−7,647	6,566	4,131	3,179	4,143	34	37	64	1.92	6.5
Lower	−11,000	2,000	2,300	1,000	2,000	0.1	0	0	0	
Upper	−5,000	8,000	5,000	3,700	4,200	35	50	180	5	

Note. Optimal = maximum a posteriori probability solution. The percentages 2.50% and 97.50% are the lower and upper boundaries of the 95% credible intervals. Lower and Upper are the bounds of the prior distribution used for the inversion. X and Y are the local coordinates of the center of RD. Local origin coordinates: longitude 91°05′W and latitude 0°49′S. Z is the depth (with respect to the caldera floor; positive downward). θ is the angle between the RD upper edge and the intersection of the RD plane with the free surface. L and W are, respectively, the length and the width. Op. is the opening. Dip is the dip angle. Strike is the strike angle (see Nikkhoo et al., 2017 for a better explanation of all these parameters). ΔV is the volume change calculated with the formula $\Delta V = L * W *$ Op. RD = rectangular dislocation.

solutions converge toward a sill that is rotated about an axis orthogonal to it (ωX parameter, see Nikkhoo et al., 2017 for details). Using the RD, we obtained solutions (Figures 4k–4n and Table 2) that are similar to the CDM, with inversions that converged for an inclined (>30°) sheet, whose center lies at 2.2 ± 0.09 km below the southern caldera floor. The opening is 0.86 ± 0.09 m, with an estimated ΔV of 7.1 (±0.6) × 10^{-3} km^3, corresponding to an average injection rate of 2.5 ± 0.3 × 10^{-3} km^3/year.

As the intracaldera fault bounds the uplifting area (Figure 3a), we tested a combination of a slipping RD and a CDM/RD inflating sill. For the RD fault, we set the angle $\theta = 0$, so that the two uppermost corners of the fault are at the same depth. In this configuration, the RD model becomes equal to that of Okada (1985) (Nikkhoo et al., 2017). Caldera inner ring faults are generally high-angle outward dipping (Acocella, 2007, and references therein). Therefore, we imposed a high dip angle (80°) and an outward dipping geometry. We also tested shallower dip angles (e.g., 70°) but obtained similar results (Figure S3 and Table S2), implying that our data cannot fully constrain high dip angles. As for the fault length (L) and width (W), we set the prior PDFs so that a realistic aspect ratio $L/W < 5$ (Leonard, 2010) could be maintained (Table 1).

In the case of the RD fault + CDM sill, the Bayesian analysis converged for a rectangular normal fault with uniform dip-slip of 0.53 ± 0.23 m, whose center lies at 0.96 ± 0.11 km below the caldera floor (Figures 4g–4j and Table 1). This fault is combined with a CDM sill, with opening of 0.6 ± 0.08 m, whose center is at 2.17 ± 0.15 km below the southern caldera floor. With this source combination the rotational parameter ωX shows a significant decrease with respect to the CDM solution without the fault. The estimated ΔV is 8.55 ± 1.05 × 10^{-3} km^3 and the corresponding rate is 3 ± 0.5 × 10^{-3} km^3/year, which are slightly lower than that estimated in the CDM solution without the fault. As for the RD fault + RD sill model, we obtained convergence for a rectangular normal fault with uniform dip-slip of 0.54 ± 0.20 m. The center of the fault is at 0.89 ± 0.08 km below the caldera floor (Figures 4o–4r and Table 2), the RD sill has 0.6 ± 0.07 m of opening, and its center is at 2.20 ± 0.14 km below the southern caldera floor. This RD sheet is less inclined (<30°) than in solutions without the fault and can be properly classified as a sill (Stephens et al., 2017). The estimated ΔV is 7.4 ± 0.7 × 10^{-3} km^3 (injection rate of 2.55 ± 0.35 × 10^{-3} km^3/year), similar to that estimated without the fault and ~12% lower than that estimated by the model RD fault + CDM sill.

For the second deformation episode we tested both a combination of two CDMs and a combination of two RDs sources to test the possibility of simulating displacements from a deflating source and a lateral intrusion. We set prior PDFs for the length and width of the sills so that an aspect ratio >1/6 is maintained. Lower aspect ratios are considered to be less realistic, since sills tend to have tabular geometries with aspect ratios >1/6 (Thomson & Hutton, 2004; Currier et al., 2017). Furthermore, this aspect ratio is consistent with that of the first event (Tables 1 and 2) and of sills emplaced at the other western Galápagos calderas of Sierra Negra, Fernandina, and Wolf (Bagnardi et al., 2013; Jónsson et al., 2005; Xu et al., 2016).

In the case of two CDMs, the inversion converged for a first sill/inclined sheet, located approximately in the same position of the previously inflated sill (Figure S4), with a contraction (or closure) of −0.37 ± 0.15 m, and a second rectangular sill placed below the western portion of the caldera with positive opening of

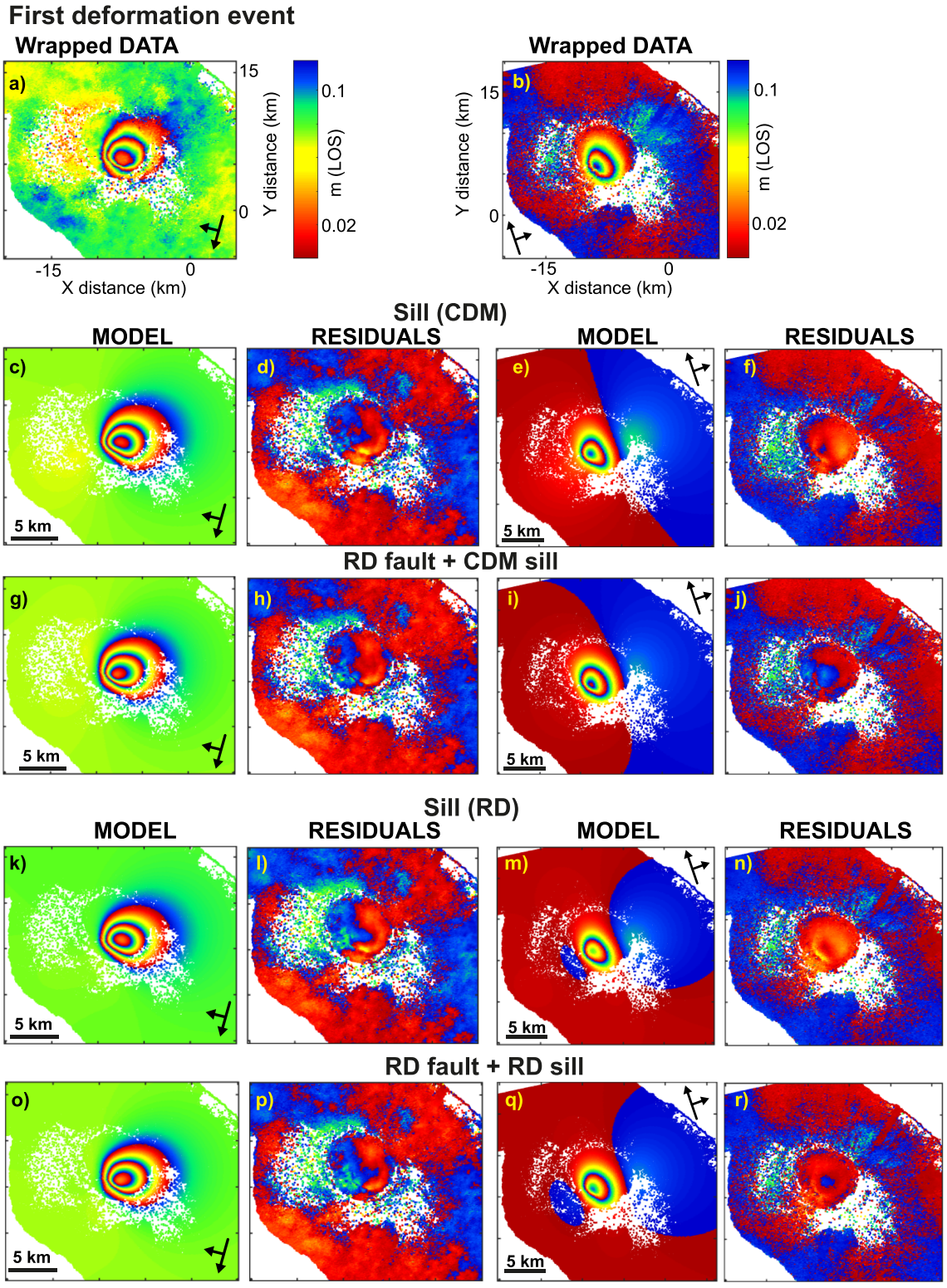

Figure 4. Wrapped ALOS-1 LOS displacements (a) for descending track 474 (January 2007 to January 2010), and (b) for ascending track 133 (January 2007 to October 2009). Each fringe (full color cycle) represents 11.8 cm of LOS displacement. Local origin coordinates: longitude 91°05′W and latitude 0°49′S. Predicted displacements (c and e) for the CDM, (g and i) for the CDM + RD fault model, (k and m) for the RD model, and (o and q) for the RD fault + RD model, using the maximum a posteriori probability solutions. Panels (d), (f), (h), (j), (l), (n), (p), and (r) show the relative residuals. LOS = line-of-sight; CDM = compound dislocation model; RD = rectangular dislocation.

0.35 ± 0.22 m. The corresponding volume changes are $-3.8 \pm 1.5 \times 10^{-3}$ km^3 (deflation rate $-7 \pm 3 \times 10^{-3}$ km^3/year) for the deflating sill and $3.15 \pm 1.45 \times 10^{-3}$ km^3 (inflation rate of $6 \pm 3 \times 10^{-3}$ km^3/year) for the inflated sill; therefore, the deflated and inflated sills of the second deformation event yield similar volume variations (Figures 5a–5f and Table 2). The inner edge of the inflating sill partially overlaps that of the deflating sill (Figure S5).

In the case of two RDs (Figures 5g–5l and Table 2), the geometry and position of the sources are similar to those from the solution with two CDMs. The deflating sill has a contraction of −0.48 ± 0.23 m, with a corresponding volume loss of $-2.3 \pm 0.7 \times 10^{-3}$ km^3 (deflation rate $-4.25 \pm 1.75 \times 10^{-3}$ km^3/year), while the inflating sill has an opening of 0.58 ± 0.38 m, with a volume increase of $2.35 \pm 0.85 \times 10^{-3}$ km^3 (rate of $4.4 \pm 2 \times 10^{-3}$ km^3/year), again comparable to the volume lost by the deflating sill.

Confidence intervals for the model parameters, for both the CDM and RD solutions, are broader than in the first event, likely due to a lower amplitude of the deformation signal leading to a lower signal-to-noise ratio in the data, with some parameters that remain poorly constrained by this analysis (Tables 1 and 2). As for the depths of the two sill centroids in both the RD and CDM models, the 95% confidence intervals only partially overlap, especially in the RD model where the center of the inflating sill tends to be deeper than that of the deflating one. However, such difference may be due to the ~150-m elevation change between the two areas under which the sills are emplaced (Lisowski, 2007), an effect for which we do not correct for in our half-space modeling approach.

Finally, we inverted data spanning the third deformation event using a RD model (Figure 6). Likely due to the low-magnitude deformation signal and to the single viewing geometry (ascending), the geometric parameters of the RD source are not well constrained (Table 3). However, the narrower range of solutions of the ΔV ($4.45 \pm 2.05 \times 10^{-3}$ km^3, Table 3) indicates this is because the parameters on which the ΔV depends trade off against each other (Figure S6). The corresponding injection rate is $5.85 \pm 2.75 \times 10^{-3}$ km^3/year, which is ~57% higher than the injection rate of the first deformation event and ~25% higher than that of the inflated sill in the second event. The depth of the center of the RD source is at 3.4 ± 0.7 km below the caldera floor.

5. Discussion

5.1. Interpretation of the Three Deformation Events

From the analysis and modeling of InSAR data, we infer that Alcedo experienced a phase of noneruptive unrest between 2007 and 2011, which can be divided into three main events.

We model the first deformation event as either due to an inflating sill or the combination of an inflating sill and reactivation of the southern intracaldera fault. In both cases, the estimated volume changes are similar. However, solutions that include the fault better reproduce the observed asymmetric deformation, especially on the ALOS-1 ascending track. Models that include the fault also converge toward a more horizontal sill geometry, as the fault accounts for part of the asymmetric deformation, as for example previously observed at Sierra Negra (Jónsson, 2009). Since this fault has been interpreted as a preexisting caldera fault (Geist et al., 1994), we modeled it using the typical outward dipping geometry (Acocella, 2007). However, we cannot exclude any inward dipping geometry, as inferred for the 2005 uplift of Sierra Negra (Jónsson, 2009). In any case, even when using an 80° inward dipping fault, we obtain similar results (Figure S7 and Table S3).

The second deformation event is consistent with the partial emptying of the previously inflated sill (~44% of contraction of the previously intruded volume for the CDM, ~30% for the RD) and the intrusion of a sill in the western caldera. Other processes such as cooling and crystallization of previously emplaced magma are less probable since they could not easily explain such a rapid (<6 months) and significant (~30–44%) volume loss (Caricchi et al., 2014). These processes would also not account for the contemporaneous uplift of the western caldera rim. Similarly, viscoelastic relaxation should not play an important role during this deflationary event, as this mechanism would require a period of transition, from uplift to subsidence, characterized by a decrease in the uplift rate (Newman et al., 2006). Such transition does not seem to occur at Alcedo, where the InSAR data show a sudden change from uplift to subsidence. The similar volumes of the deflating sill and that of the inflated sill, as well as their juxtaposition, suggest a lateral propagation of the sill formed

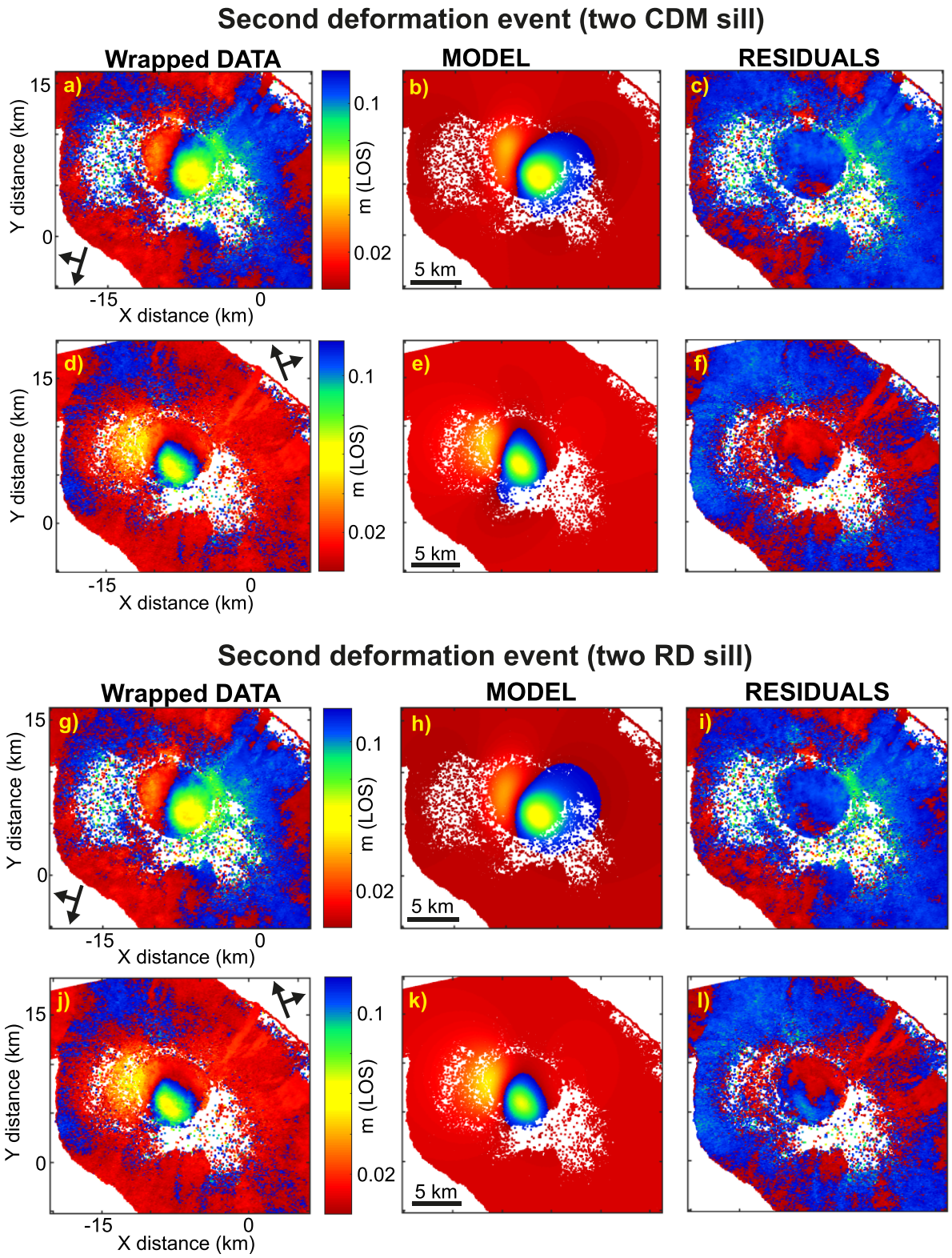

Figure 5. Wrapped ALOS-1 LOS displacements (a and g) for descending track 474 (January 2010 to July 2010) and (d and j) for ascending track 133 (October 2009 to June 2010). Each fringe (full color cycle) represents 11.8 cm of LOS displacement. Local origin coordinates: longitude 91°05'W and latitude 0°49'S. (b and e) Predicted displacements for two CDMs using the maximum a posteriori probability solution and (c and f) the related residuals. (h and k) Predicted displacements for two RD models using the maximum a posteriori probability solution and (i and l) the related residuals. LOS = line-of-sight; CDM = compound dislocation model; RD = rectangular dislocation.

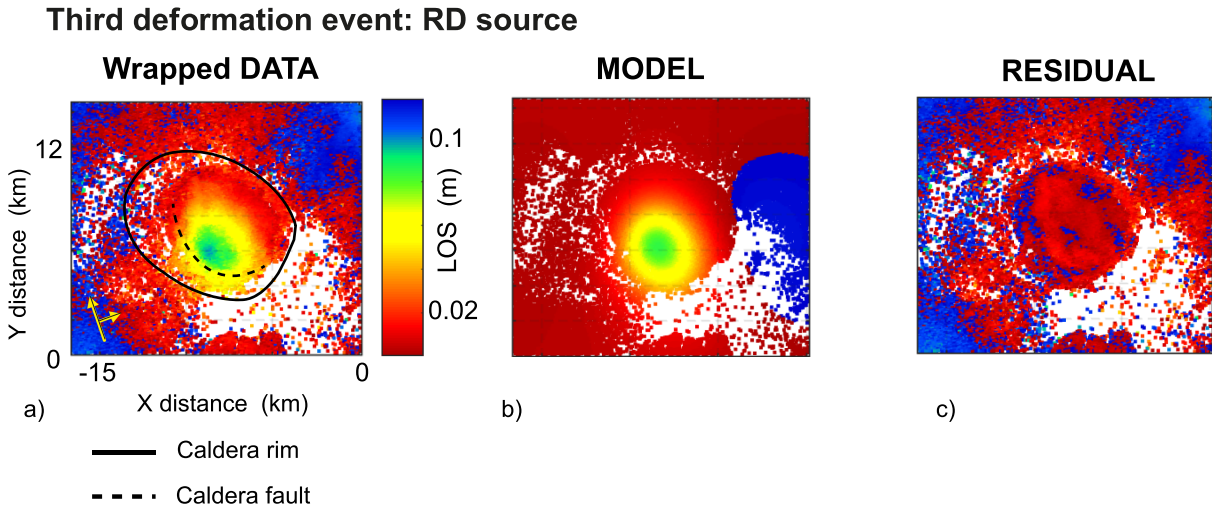

Figure 6. (a) Wrapped ALOS-1 LOS displacements for ascending track 133 (June 2010 and March 2011). Each fringe (full color cycle) represents 11.8 cm of LOS displacement. Local origin coordinates: longitude 91°05′W and latitude 0°49′S. (b) Predicted displacements for a RD model using the maximum a posteriori probability solution. (c) Related residual. LOS = line-of-sight; RD = rectangular dislocation.

during the first event from below the caldera (Figure 7). Since in some of our solutions the inflated sill is deeper than the deflating one, some downward migration of magma from the deflating sill may have occurred during the lateral propagation, as proposed at larger scale for the 2001–2002 subsidence occurred at Sierra Negra (Geist et al., 2006).

This process has been observed previously, though reaching a much farther lateral propagation, at other western Galápagos calderas, such as Fernandina (Bagnardi et al., 2013), and may have been controlled by the stress field that results from the topographic unloading due to the caldera depression (Corbi et al., 2015, and references therein). However, in the case of Alcedo, the lateral propagation of the sill was limited (only a few kilometers) and the intrusion aborted soon, without any eruption, near the caldera boundary, where important stress changes occur (Corbi et al., 2015, and references therein). We interpret this aborted lateral magma propagation to the discontinuity in the supply of magma from depth. This event underlies the importance of a continuous supply in the propagation of magma to the surface and feed eruptions.

Finally, the third deformation event is compatible with the inflation of a source approximately located in the same position as the source that inflated during the first event and deflated during the second event (Figure 7). Even if the source depth is not as well constrained, its 95% confidence interval (Table 3) shows only a partial overlap with previous sources, suggesting that this intrusion may be emplaced below the one that caused the first episode of uplift. The positive volume change during the third event corresponds to ~60% of that observed during the first event.

We can explain the asymmetric uplift during the first event as the combined effect of magma addition to the source and fault reactivation. The asymmetric deformation also observed during the second and third events suggests that the same fault, even though not included in our models, may have been subsequently active. The deformations at Alcedo from 1992 to 2001 (Amelung et al., 2000; Hooper et al., 2007), occurred in the same area and showed the same asymmetrical pattern, suggesting that this fault was active also during the previous unrest.

5.2. A General Model for Alcedo

According to the general evolutionary model for western Galápagos volcanoes, Alcedo may be in a dying phase and its magmatic system may be characterized by a mush zone that should be no longer in a thermal steady state and cooler with respect to that of the nearby calderas (Geist et al., 2014; Harpp & Geist, 2018). Geist et al. (1994) suggested, on morphological and geologic evidence, that the shallower portion of the magmatic system of Alcedo lies now below the southern part of the caldera, where Alcedo also hosts a shallow (located above sea level) hydrothermal system (Goff et al., 2000). Our data, as well as the geodetic data from 1992 to 2001 (Amelung et al., 2000; Hooper et al., 2007), support this hypothesis, suggesting that this shorter-

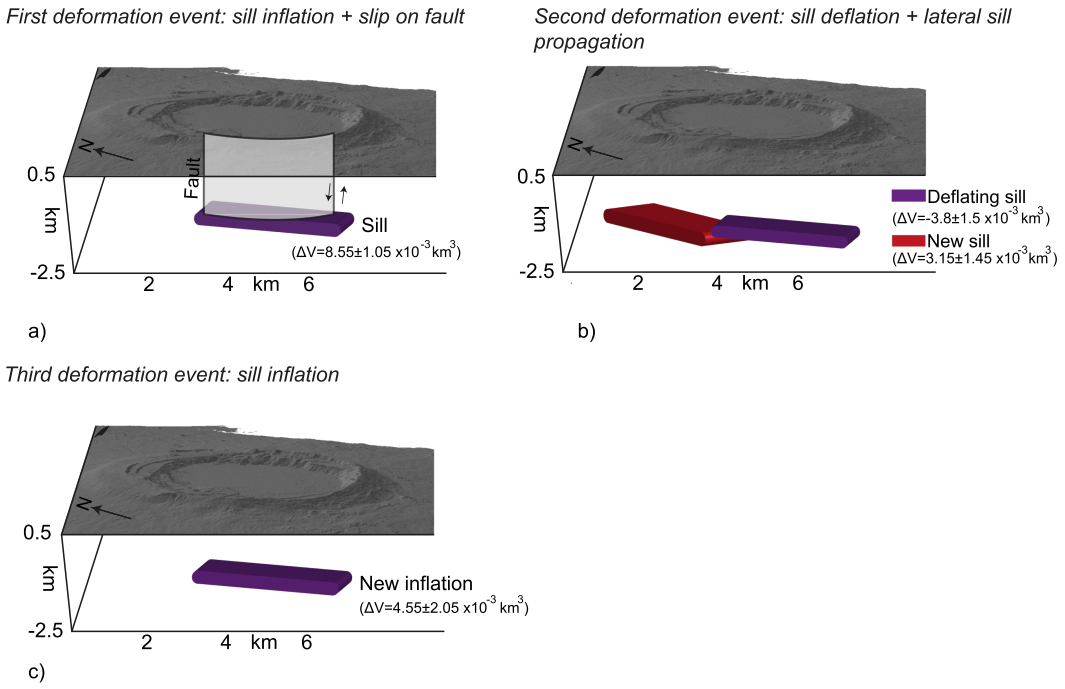

Figure 7. Conceptual models summarizing the three deformation events at Alcedo. (a) First event with sill inflation and reactivation of an intracaldera fault. (b) Second event: lateral magma propagation and sill deflation. (c) Third event: sill reinflation.

term deformation (years long) focuses in the southern part of the caldera. The 2- to 3-km depth of the sills centroids in our study is also consistent with the depth of the source that caused the subsidence of the southern part of the caldera from 1997 to 2001 (Hooper et al., 2007). Furthermore, this depth agrees with that of the top of the shallow magmatic systems of the nearby calderas at Fernandina, Sierra Negra, and Wolf (from 1 to 3 km depth below the caldera; Bagnardi et al., 2013; Jónsson, 2009; Stock et al., 2018). Such depths are more consistent with those of magmatic sources than with that of the shallow hydrothermal system of Alcedo. However, we cannot exclude a minor contribution of the hydrothermal system to the total deformation signal, which could be possibly triggered by the inflow of new magmatic fluids linked to the new intrusions (Hurwitz et al., 2007). Our observations suggests that sill inflation during the first and third events were related to the replenishment of the shallow magmatic system, possibly as intrusions within the magmatic mush, from which the magma propagated laterally (during the second event). However, not only did the lateral propagation of magma not result in an eruption, but it also terminated as a stalled intrusion at a short distance. This aborted lateral propagation of the sill is interpreted as being due to the fact that the magmatic system was not being replenished during the second deformation event, or was being replenished at much lower rates, as indicated by the similar volume changes of the inflating laterally propagating sill and the deflating subcaldera sill. The second event at Alcedo thus may provide an interesting example of magma propagation aborted by the lack of continuous replenishment of the main shallow reservoir. Pressure decrease in the feeding sill and magma solidification in the propagating sill (Rivalta, 2010; Rubin, 1995) may both have caused the arrest of the laterally propagating sill, although stress changes caused by the morphology of the caldera rim may have also contributed to its arrest (Corbi et al., 2015).

Our data suggest that the sill responsible for the third event may have been emplaced below that of the first event, even if replenishment of the former sill cannot be excluded. Thus, the intrusive system of Alcedo may grow through the emplacement of stacked sills, possibly within the magmatic mush, and not necessarily by the replenishment of the same sill. Our results allow for the possibility that the stacked sills touch each other. This is consistent with the fact that a partially molten magma body can act as a rheological barrier for the new intrusion, hindering its upward propagation (Galetto et al., 2017), as also confirmed by some eroded laccoliths and plutons (Leuthold et al., 2012; Miller et al., 2011).

A further insight obtained from the analysis of surface deformation data during recent decades is its possible relation with the longer-term (decades at least) behavior of the caldera. During the time period here analyzed, as well as between 1992 and 2001 (Amelung et al., 2000; Hooper et al., 2007, the amount of uplift was greater than that of subsidence, resulting in a net asymmetric uplift of the southern caldera floor. This asymmetric uplift matches with the morphology of the southern part of the caldera, which shows ~30 m of trapdoor uplift (Figure 1) confined by the same intracaldera fault that was active during our first event and probably the subsequent ones. We speculate that the trapdoor uplift geodetically detected here may represent the nearly instantaneous expression of a decades-to-centuries long process of weak resurgence at Alcedo (Geist et al., 1994). These geodetically detected uplift episodes would thus provide the opportunity to observe a specific moment of growth of a resurgence, implying that resurgence is a discontinuous and incremental process, also involving episodes of limited subsidence. This in turn implies that resurgence results from the repeated and cumulative emplacement of shallow intrusions within the mushy magmatic system, each with its distinct history, probably supported by the thermal state of the crust, as suggested for the Campi Flegrei caldera (Amoruso et al., 2017). The weak resurgence of Alcedo would be related to its relatively late evolutionary stage (dying phase; Geist et al., 2014), characterized by a cooling shallow magmatic system shifted toward a more felsic composition and, as also witnessed during the second deformation event, by a discontinuous magma supply. All these features are characteristic of most of the resurgent calderas and could promote the accumulation of magma at depth and resurgence (Galetto et al., 2017). The trapdoor resurgence at Alcedo is also similar in shape (asymmetric) and extent (several tens of meters) to that observed at nearby Sierra Negra (Galetto et al., 2017, and references therein) and is among the very rare examples of resurgence observed at basaltic calderas. However, resurgence at the caldera of Alcedo grows with lower (up to 1 order of magnitude) rates than at Sierra Negra (Geist et al., 2006), which could be related to the much lower magma supply to Alcedo.

Therefore, the noneruptive unrest at Alcedo described here, as well as that which occurred between 1992 and 2001, may represent short-term intrusion episodes related to a longer-term resurgence. These geodetically observed episodes provide the unusual opportunity to witness the short-term stages of growth of a rare resurgence in a basaltic caldera.

6. Conclusions

We have identified two distinct episodes of shallow sill emplacement at Alcedo, triggering a net uplift of ~26 cm from January 2007 to January 2010 and from June 2010 to March 2011. In between (January 2010 to June 2010), the previously intruded sill, even though not replenished, migrated laterally, without erupting. We relate the arrest of the sill to the discontinuous supply of magma, supported by our estimates of the volume variations of the deflated and inflated sills in the first half of 2010. This indicates the importance of the continuity in the supply of magma to have eruptive unrest.

We also highlight that all the deformation episodes from 1992 to 2011 occurred in the southern caldera floor and showed the same asymmetric pattern, bordered by the same intracaldera ring fault to the south. This shorter-term deformation is consistent in location (southern part of the caldera) and shape (asymmetry) with the longer-term one deduced from geologic evidence, highlighting a weak (~30 m uplift) resurgence. This consistency suggests that Alcedo has been experiencing incremental and discontinuous episodes of growth of its resurgent block, related to the emplacement of multiple sills, a rare occurrence to witness at basaltic calderas. Future studies should investigate if the intrusive magmatic systems of the other western Galápagos calderas also grow through the emplacement of multiple stacked sills, as inferred at Alcedo.

Acknowledgments
We thank K. Spaans, R. Amey, and J. Giniaux for their helpful suggestions. We also thank D. Geist and an anonymous reviewer for the constructive suggestions. M. B. was supported by the NERC Centre for the Observation and Modelling of Earthquakes, Volcanoes and Tectonics (COMET) and by an appointment to the NASA Postdoctoral Program at the Jet Propulsion Laboratory, administered by the Universities Space and Research Association (USRA) through a contract with NASA. The grant to the Department of Science, Roma Tre University (MIUR-Italy Dipartimenti di Eccellenza, ARTICOLO 1, COMMI 314–337 LEGGE 232/2016) is gratefully acknowledged. The Envisat data are distributed by the European Space Agency (ESA) via ESA's Virtual Archive (http://eo-virtual-archive4.esa.int/) in the framework of the Geohazard Supersites and Natural Laboratory initiative. The ALOS-PALSAR data are copyright JAXA/METI. All the other information that support this study are in the supporting information file.

References

Acocella, V. (2007). Understanding caldera structure and development: An overview of analogue models compared to natural calderas. *Earth-Science Reviews*, *85*(3-4), 125–160. https://doi.org/10.1016/j.earscirev.2007.08.004.

Acocella, V., Di Lorenzo, R., Newhall, C., & Scandone, R. (2015). An overview of recent (1988 to 2014) caldera unrest: Knowledge and perspectives. *Reviews of Geophysics*, *53*, 896–955. https://doi.org/10.1002/2015RG000492

Amelung, F., Jónsson, S., Zebker, H., & Segall, P. (2000). Widespread uplift and 'trapdoor' faulting on Galápagos volcanoes observed with radar interferometry. *Nature*, *407*(6807), 993–996. https://doi.org/10.1038/35039604

Amoruso, A., Crescentini, L., D'Antonio, M., & Acocella, V. (2017). Thermally-assisted magma emplacement explains restless calderas. *Scientific Reports*, *7*, 7948. https://doi.org/10.1038/s41598-017-08638-y

Bagnardi, M., Amelung, F., & Poland, M. P. (2013). A new model for the growth of basaltic shields based on deformation of Fernandina Volcano, Galápagos Islands. *Earth and Planetary Science Letters*, *377-378*, 358–366. https://doi.org/10.1016/j.epsl.2013.07.016

Bagnardi, M., & Hooper, A. (2018). Inversion of surface deformation data for rapid estimates of source parameters and uncertainties: A Bayesian approach. *Geochemistry, Geophysics, Geosystems*, *19*, 2194–2211. https://doi.org/10.1029/2018GC007585

Biggs, J., Ebmeier, S. K., Aspinall, W. P., Lu, Z., Pritchard, M. E., Sparks, R. S. J., & Mather, T. A. (2014). Global link between deformation and volcanic eruption quantified by satellite imagery. *Nature Communications*, *5*, 3471. https://doi.org/10.1038/ncomms4471

Biggs, J., & Pritchard, M. E. (2017). Global volcano monitoring: What does it mean when volcanoes deform? *Elements*, *13*, 17–22. https://doi.org/10.2113/gselements.13.1.17

Canales, J. P., Dañobeitia, J. J., Detrick, R. S., Hooft, E. E., Bartolomé, R., & Naar, D. F. (1997). Variations in axial morphology along the Galápagos spreading center and the influence of the Galápagos hotspot. *Journal of Geophysical Research*, *102*(B12), 27,341–27,354. https://doi.org/10.1029/97JB01633

Canales, J. P., Ito, G., Detrick, R. S., & Sinton, J. (2002). Crustal thickness along the western Galápagos spreading center and the compensation of the Galápagos hotspot swell. *Earth and Planetary Science Letters*, *203*(1), 311–327. https://doi.org/10.1016/S0012-821X(02)00843-9

Caricchi, L., Biggs, J., Annen, C., & Ebmeier, S. (2014). The influence of cooling, crystallisation and re-melting on the interpretation of geodetic signals in volcanic systems. *Earth and Planetary Science Letters*, *388*, 166–174. https://doi.org/10.1016/j.epsl.2013.12.002

Corbi, F., Rivalta, E., Pinel, V., Maccaferri, F., Bagnardi, M., & Acocella, V. (2015). How caldera collapse shapes the shallow emplacement and transfer of magma in active volcanoes. *Earth and Planetary Science Letters*, *431*, 287–293. https://doi.org/10.1016/j.epsl.2015.09.028

Currier, R. M., Forsythe, P., Grossmeier, C., Laliberte, M., & Yagle, B. (2017). Experiments on the evolution of laccolith morphology in plan-view. *Journal of Volcanology and Geothermal Research*, *336*, 155–167. https://doi.org/10.1016/j.jvolgeores.2017.02.017

Decriem, J., Árnadóttir, T., Hooper, A., Geirsson, H., Sigmundsson, F., Keiding, M., et al. (2010). The 2008 May 29 earthquake doublet in SW Iceland. *Geophysical Journal International*, *181*, 1128–1146. https://doi.org/10.1111/j.1365-246X.2010.04565.x

Degruyter, W., & Huber, C. (2014). A model for eruption frequency of upper crustal silicic magma chambers. *Earth and Planetary Science Letters*, *403*, 117–130. https://doi.org/10.1016/j.epsl.2014.06.047

Dvorak, J. J., & Dzurisin, D. (1997). Volcano geodesy: The search for magma reservoirs and the formation of eruptive vents. *Reviews of Geophysics*, *35*(3), 343–384. https://doi.org/10.1029/97RG00070

Farr, T. G., Rosen, P. A., Caro, E., Crippen, R., Duren, R., Hensley, S., et al. (2007). The shuttle radar topography mission. *Reviews of Geophysics*, *45*, RG2004. https://doi.org/10.1029/2005RG000183

Feighner, M. A., & Richards, M. A. (1994). Lithospheric structure and compensation mechanisms of the Galápagos Archipelago. *Journal of Geophysical Research*, *99*(B4), 6711–6729. https://doi.org/10.1029/93JB03360

Galetto, F., Acocella, V., & Caricchi, L. (2017). Caldera resurgence driven by magma viscosity contrasts. *Nature Communications*, *8*, 1750. https://doi.org/10.1038/s41467-017-01632-y

Geist, D., Chadwick, W., & Johnson, D. (2006). Results from new GPS and gravity monitoring networks at Fernandina and Sierra Negra Volcanoes, Galápagos, 2000–2002. *Journal of Volcanology and Geothermal Research*, *150*, 79–97. https://doi.org/10.1016/j.jvolgeores.2005.07.003

Geist, D., Howard, K. A., Jellinek, A. M., & Rayder, S. (1994). The volcanic history of Volcán Alcedo, Galápagos Archipelago: A case study of rhyolitic oceanic volcanism. *Bulletin of Volcanology*, *56*(4), 243–260. https://doi.org/10.1007/BF00302078

Geist, D., Howard, K. A., & Larson, P. (1995). The generation of oceanic rhyolites by crystal fractionation: The basalt-rhyolite association at Volcán Alcedo, Galápagos Archipelago. *Journal of Petrology*, *36*(4), 965–982. https://doi.org/10.1093/petrology/36.4.965

Geist, D. J., Bergantz, G., & Chadwick, W. W. Jr. (2014). Galápagos magma chambers. In K. S. Harpp, E. Mittelstaedt, N. d'Ozouville, & D. W. Graham (Eds.), *The Galápagos: A natural laboratory for the Earth sciences* (Vol. 204, pp. 55–70). Hoboken, NJ: John Wiley & Sons. https://doi.org/10.1002/9781118852538.ch5

Gibson, S. A., & Geist, D. (2010). Geochemical and geophysical estimates of lithospheric thickness variation beneath Galápagos. *Earth and Planetary Science Letters*, *300*, 275–286. https://doi.org/10.1016/j.epsl.2010.10.002

Goff, F., McMurtry, G. M., Counce, D., Simac, J. A., Roldán-Manzo, A. R., & Hilton, D. R. (2000). Contrasting hydrothermal activity at Sierra Negra and Alcedo Volcanoes, Galápagos Archipelago, Ecuador. *Bulletin of Volcanology*, *62*(1), 34–52. https://doi.org/10.1007/s004450050289

Green, J. R. (1994). Recent activity in Alcedo Volcano, Isabela Island. *Noticias de Galápagos*, *54*, 11–12.

Gudmundsson, M. T., Jónsdóttir, K., Hooper, A., Holohan, E. P., Halldórsson, S. A., Ófeigsson, B. G., et al. (2016). Gradual caldera collapse at Bárdarbunga Volcano, Iceland, regulated by lateral magma outflow. *Science*, *353*, aaf8988. http://doi.org/10.1126/science.aaf8988

Harpp, K. S., & Geist, D. J. (2018). The evolution of Galápagos volcanoes: An alternative prospective. *Frontiers in Earth Science*, *6*, 50. https://doi.org/10.3389/feart.2018.00050

Hooft, E. E., Toomey, D. R., & Solomon, S. C. (2003). Anomalously thin transition zone beneath the Galápagos hotspot. *Earth and Planetary Science Letters*, *216*(1-2), 55–64. https://doi.org/10.1016/S0012-821X(03)00517-X

Hooper, A. (2008). A multi-temporal InSAR method incorporating both persistent scatterer and small baseline approaches. *Geophysical Research Letters*, *35*, L16302. https://doi.org/10.1029/2008GL034654

Hooper, A., Bekaert, D., Spaans, K., & Ankan, M. (2012). Recent advances in SAR interferometry time series analysis for measuring crustal deformations. *Tectonophysics*, *514-517*, 1–13. https://doi.org/10.1016/j.tecto.2011.10.013

Hooper, A., Segall, P., & Zebker, H. (2007). Persistent scatterer interferometric synthetic aperture radar for crustal deformation analysis, with application to Volcán Alcedo, Galápagos. *Journal of Geophysical Research*, *112*, B07407. https://doi.org/10.1029/2006JB004763

Howard, K. A., Simkin, T., Geist, D. J., Merlen, G., & Nolf, B. (2018). Large hydromagmatic eruption related to Fernandina Volcano's 1968 caldera collapse—Deposits, landforms, and ecosystem recovery. In M. Poland, M. O. Garcia, V. E. Camp, & A. Grunder (Eds.), *Field volcanology: A tribute to the distinguished career of Don Swanson* (Vol. 538, pp. 385–408). Geological Society of America. https://doi.org/10.1130/2018.2538(18)

Huppert, H. E., & Woods, A. W. (2002). The role of volatiles in magma chamber dynamics. *Nature*, *420*(6915), 493–495. https://doi.org/10.1038/nature01211

Hurwitz, S., Christiansen, L. B., & Hsieh, P. A. (2007). Hydrothermal fluid flow and deformation in large calderas: Inferences from numerical simulations. *Journal of Geophysical Research*, *112*, B02206. https://doi.org/10.1029/2006JB004689

Jellinek, A. M., & DePaolo, D. J. (2003). A model for the origin of large silicic magma chambers: Precursors of caldera-forming eruptions. *Bulletin of Volcanology*, *65*(5), 363–381. https://doi.org/10.1007/s00445-003-0277-y

Jónsson, S. (2009). Stress interaction between magma accumulation and trapdoor faulting on Sierra Negra Volcano, Galápagos. *Tectonophysics*, *471*, 36–44. https://doi.org/10.1016/j.tecto.2008.08.005

Jónsson, S., Zebker, H., & Amelung, F. (2005). On trapdoor faulting at Sierra Negra Volcano, Galapagos. *Journal of Volcanology and Geothermal Research*, *144*, 59–71. https://doi.org/10.1016/j.jvolgeores.2004.11.029

Leonard, M. (2010). Earthquake fault scaling: Self-consistent relating of rupture length, width, average displacement, and moment release. *Bulletin of the Seismological Society of America*, *100*, 1971–1988. https://doi.org/10.1785/0120090189

Leuthold, J., Müntener, O., Baumgartner, L. P., Putlitz, B., Ovtcharova, M., & Schaltegger, U. (2012). Time resolved construction of a bimodal laccolith (Torres del Paine, Patagonia). *Earth and Planetary Science Letters*, *325*, 85–92. https://doi.org/10.1016/j.epsl.2012.01.032

Lisowski, M. (2007). *Analytical volcano deformation source models*, *Volcano deformation* (pp. 279–304). Berlin, Heidelberg: Springer. https://doi.org/10.1007/978-3-540-49302-0_8

McTigue, D. F. (1987). Elastic stress and deformation near a finite spherical magma body: Resolution of the point source paradox. *Journal of Geophysical Research*, *92*(B12), 12931. https://doi.org/10.1029/JB092iB12p12931

Miller, C. F., Furbish, D. J., Walker, B. A., Claiborne, L. L., Koteas, G. C., Bleick, H. A., & Miller, J. S. (2011). Growth of plutons by incremental emplacement of sheets in crystal-rich host: Evidence from Miocene intrusions of the Colorado River region, Nevada, USA. *Tectonophysics*, *500*, 65–77. https://doi.org/10.1016/j.tecto.2009.07.011

Mittelstaedt, E., Soule, S., Harpp, K., Fornari, D., McKee, C., Tivey, M., Geist, D., et al. (2012). Multiple expressions of plume-ridge interaction in the Galápagos: Volcanic lineaments and ridge jumps. *Geochemistry, Geophysics, Geosystems*, *13*, Q05018. https://doi.org/10.1029/2012GC004093

Mogi, K. (1958). Relations between the eruptions of various volcanoes and the deformations of the ground surfaces around them. *Bulletin of the Earthquake Research Institute*, *36*, 99–134.

Mouginis-Mark, P. J., Rowland, S. K., & Garbeil, H. (1996). Slopes of western Galápagos volcanoes from airborne interferometric radar. *Geophysical Research Letters*, *23*(25), 3767–3770. https://doi.org/10.1029/96GL03280

Munro, D. C., & Rowland, S. K. (1996). Caldera morphology in the western Galápagos and implications for volcano eruptive behavior and mechanisms of caldera formation. *Journal of Volcanology and Geothermal Research*, *72*(1-2), 85–100. https://doi.org/10.1016/0377-0273(95)00076-3

Naumann, T., & Geist, D. (2000). Physical volcanology and structural development of Cerro Azul Volcano, Isabela Island, Galápagos: Implications for the development of Galápagos-type shield volcanoes. *Bulletin of Volcanology*, *61*(8), 497–514. https://doi.org/10.1007/s004450050001

Newhall, C. G., & Dzurisin, D. (1988). *Historical unrest at large calderas of the world*, (Vol. 1-2, pp. 1108). Washington: U.S. Geol. Surv. Bull., 1855.

Newman, A. V., Dixon, T. H., & Gourmelen, N. (2006). A four-dimensional viscoelastic deformation model for Long Valley Caldera, California, between 1995 and 2000. *Journal of Volcanology and Geothermal Research*, *150*, 244–269. https://doi.org/10.1016/j.jvolgeores.2005.07.017

Nikkhoo, M., Walter, T. R., Lundgren, P. R., & Prats-Iraola, P. (2017). Compound dislocation models (CDMs) for volcano deformation analyses. *Geophysical Journal International*, *208*, 877–894. https://doi.org/10.1093/gji/ggw427

Nordlie, B. E. (1973). Morphology and structure of the western Galápagos volcanoes and a model for their origin. *Geological Society of America Bulletin*, *84*(9), 2931–2956. https://doi.org/10.1130/0016-7606(1973)84<2931:MASOTW>2.0.CO;2

Okada, Y. (1985). Surface deformation due to shear and tensile faults in a half-space. *Bulletin of the Seismological Society of America*, *75*, 1135–1154.

Rivalta, E. (2010). Evidence that coupling to magma chambers controls the volume history and velocity of laterally propagating intrusions. *Journal of Geophysical Research*, *115*, B07203. https://doi.org/10.1029/2009JB006922

Rosen, P. A., Gurrola, E., Sacco, G. F., & Zebker, H. (2012). The InSAR scientific computing environment. In *Synthetic Aperture Radar, 2012. EUSAR. 9th European Conference on* (pp. 730-733). VDE.

Rubin, A. M. (1995). Propagation of magma-filled cracks. *Annual Review of Earth and Planetary Sciences*, *23*(1), 287–336. https://doi.org/10.1146/annurev.ea.23.050195.001443

Rychert, C. A., Harmon, N., & Ebinger, C. (2014). Receiver function imaging of lithospheric structure and the onset of melting beneath the Galápagos Archipelago. *Earth and Planetary Science Letters*, *388*, 156–165. https://doi.org/10.1016/j.epsl.2013.11.027

Sandri, L., Acocella, V., & Newhall, C. (2017). Searching for patterns in caldera unrest. *Geochemistry, Geophysics, Geosystems*, *18*, 2748–2768. https://doi.org/10.1002/2017GC006870

Stephens, T. L., Walker, R. J., Healy, D., Bubeck, A., England, R. W., & McCaffrey, K. J. (2017). Igneous sills record far-field and near-field stress interactions during volcano construction: Isle of Mull, Scotland. *Earth and Planetary Science Letters*, *478*, 159–174. https://doi.org/10.1016/j.epsl.2017.09.003

Stock, M. J., Bagnardi, M., Neave, D. A., Maclennan, J., Bernard, B., Buisman, I., et al. (2018). Integrated petrological and geophysical constraints on magma system architecture in the western Galápagos Archipelago: Insights from Wolf Volcano. *Geochemistry, Geophysics, Geosystems*, *19*, 4722–4743. https://doi.org/10.1029/2018GC007936

Thomson, K., & Hutton, D. (2004). Geometry and growth of sill complexes: Insights using 3D seismic from the North Rockall Trough. *Bulletin of Volcanology*, *66*, 364–375. https://doi.org/10.1007/s00445-003-0320-z

Villagómez, D. R., Toomey, D. R., Geist, D. J., Hooft, E. E., & Solomon, S. C. (2014). Mantle flow and multistage melting beneath the Galápagos hotspot revealed by seismic imaging. *Nature Geoscience*, *7*, 151–156. https://doi.org/10.1038/ngeo2062

Voight, B., Widiwijayanti, C., Mattioli, G., Elsworth, D., Hidayat, D., & Strutt, M. (2010). Magma-sponge hypothesis and stratovolcanoes: Case for a compressible reservoir and quasi-steady deep influx at Soufrière Hills Volcano, Montserrat. *Geophysical Research Letters*, *37*, L00E05. https://doi.org/10.1029/2009GL041732

Werner, R., Hoernle, K., Barckhausen, U., & Hauff, F. (2003). Geodynamic evolution of the Galápagos hot spot system (central east Pacific) over the past 20 my: Constraints from morphology, geochemistry, and magnetic anomalies. *Geochemistry, Geophysics, Geosystems*, *4*(12), 1108. https://doi.org/10.1029/2003GC000576

White, W. M., McBirney, A. R., & Duncan, R. A. (1993). Petrology and geochemistry of the Galápagos Islands: Portrait of a pathological mantle plume. *Journal of Geophysical Research*, *98*(B11), 19,533–19,563. https://doi.org/10.1029/93JB02018

Wright, T. J., Parsons, B. E., & Lu, Z. (2004). Toward mapping surface deformation in three dimensions using InSAR. *Geophysical Research Letters*, *31*, L01607. https://doi.org/10.1029/2003GL018827

Xu, W., Jónsson, S., Ruch, J., & Aoki, Y. (2016). The 2015 Wolf Volcano (Galápagos) eruption studied using Sentinel-1 and ALOS-2 data. *Geophysical Research Letters*, *43*, 9573–9580. https://doi.org/10.1002/2016GL069820

Yang, X. M., Davis, P. M., & Dieterich, J. H. (1988). Deformation from inflation of a dipping finite prolate spheroid in an elastic half-space as a model for volcanic stressing. *Journal of Geophysical Research*, *93*(B5), 4249–4257. https://doi.org/10.1029/JB093iB05p04249